PCCP

PAPER

Cite this: *Phys. Chem. Chem. Phys.*, 2018, **20**, 4587

Microkinetic model for reaction and diffusion of titanium interstitial atoms near a TiO_2(110) surface

Kandis Leslie Gilliard-AbdulAziz and Edmund G. Seebauer *

Received 19th November 2017,
Accepted 16th January 2018

DOI: 10.1039/c7cp07802a

rsc.li/pccp

Semiconductor surfaces provide efficient pathways for injecting native point defects into the underlying bulk. In the case of interstitial atoms in rutile, the TiO_2(110) surface exemplifies this behavior, although extended defects in the bulk such as platelets and crystallographic shear planes act as net sources or sinks depending upon specific conditions. The present work constructs a quantitative microkinetic model to describe diffusion and based upon isotopic gas–solid exchange experiments. Key activation barriers for are 0.55 eV for surface injection, 0.50 eV for site-to-site hopping diffusion, and 3.3 eV for dissociation of titanium interstitials from extended defects.

Introduction

Semiconductor surfaces that are free of bond-saturating adsorbed species provide efficient pathways for the creation and annihilation of point defects. Previous work in Si,[1,2] TiO_2[3–5] and ZnO[6,7] indicates that these pathways leads to changes in bulk defect populations that sometimes vary by orders of magnitude from literature reports and that approach thermodynamic equilibrium more closely. For the case of rutile TiO_2 heated in O_2 gas, an atomically clean (110) surface injects oxygen interstitials (O_i) at a sufficiently large rate that O_i supplants the O vacancy as the majority O-related native defect.[3,4] With Ti present in the gas from an evaporation source, the surface also injects titanium interstitials (Ti_i) at a sufficiently large rate that extended defects form in the bulk,[8] including platelets and crystallographic shear planes. The extended defects act as reservoirs of O_i and Ti_i, acting as net sources or sinks of these species depending upon specific conditions. The rich chemistry of surface–defect interaction merits attention in its own right, and manipulation of bulk defect populations provides opportunities to unravel complicated defect diffusion–reaction networks for better scientific understanding and technological advantage.

Because of the experimental challenges that accompany direct examination of point defects by imaging or spectroscopy, isotopic exchange experiments must supported by mathematical modeling to interpret the observables in terms of diffusion and reaction. Models of this kind that include surfaces are well developed only for silicon[1,2] and have been published for oxide semiconductors only recently.[5,6] The presence of two or more elements multiplies the possible varieties of point defects, as well as the permutations of reactions that may occur among the defects as well as with surfaces, lattice atoms and extended defects.

The lone published example of a microkinetic model for a semiconducting oxide that includes surface effects is for oxygen in rutile TiO_2(110).[5] That model neglects any coupling between the diffusion–reaction networks of the anion and cation, and presupposes that the lattice serves as the primary sequestration reservoir for O_i. The present work advances the understanding of the TiO_2 system by building upon that model to account for the behavior of the Ti cation, and Ti–O network coupling through extended defects that actually serve as the dominant sequestration reservoir. The model provides estimates for the activation energies and pre-exponential factors describing the injection, site-hopping diffusion, and interaction of Ti_i with extended defects. Some of these parameters have no existing counterparts in the literature. Counterintuitively, the surface concentration of injectable Ti increases with temperature, rather than decreasing as in conventional gas adsorption.

Calculation method

The approach to microkinetic modeling of defect behavior followed the approach described elsewhere.[13] Primary data originated from a gas-solid exchange method, in which rutile TiO_2(110) single crystals were annealed (550–700 °C) in isotopically labeled gas ($^{18}O_2$) and a gaseous flux of ^{46}Ti from labeled TiO_2 contained in a heated source. The O_2 gas >99% isotopically pure, and the Ti was enriched to 76.4%. Prior to isotopic exchange, specimens were annealed in natural abundance O_2 for 4 h at the selected diffusion temperature and oxygen pressure to help equilibrate defect concentrations as well as to thermally clean the surface. Specimens were subsequently annealed in $^{18}O_2$ gas for 30 min at 5×10^{-6} Torr with

Department of Chemical and Biomolecular Engineering, University of Illinois, Urbana, Illinois 61801, USA. E-mail: eseebaue@illinois.edu; Fax: +217 333-5052; Tel: +217 244-9214

simultaneous exposure to a flux of ^{46}Ti. Isotopic Ti and O profiles were measured *ex situ* with a time of flight SIMS with a 2–3 keV oxygen and cesium ion beam, respectively. Other procedural details and examples of primary data appear in ref. 8.

Ti_i represents the majority Ti-related point defect in rutile, and the majority defect overall under the conditions of the experiments. Prior work[3–5] has shown that O_i carries essentially all the oxygen diffusional flux. This dominance follows from the fact that O_i is the majority O-related defect in rutile TiO_2 under the conditions of the experiments with a clean surface in proximity, and that O_i moves more quickly than V_O. The shapes of the diffusion profiles for both elements follow from the kinetics of Ti_i and O_i injection, migration, and reaction with reservoirs such as extended defects.

The lattice may also serve as a reservoir in principle, but does not play a significant role in determining isotopic Ti profile shapes for the temperatures and timescales examined here. The reasons are subtle. First principles calculations indicate that Ti_i diffusion by exchange with nearby lattice Ti atoms[9] represents the lowest energy pathway, compared with a direct pathway involving no exchange. Thus, the mean path length of a labeled Ti_i atom before lattice sequestration is only one atomic diameter. Yet experimental profiles show these mean path lengths range from 10 to 1000 nm. Moreover, the barriers for Ti_i hopping are rather low (0.35 eV), so that many hops occur during the diffusion experiments that last on the order of an hour. Therefore, labeled atoms do exchange into the lattice and remain there for very brief intervals, but that sequestration time is so short that the experiments cannot distinguish that process from a hypothetical low-barrier direct pathway. The experiments still yield the exponentially shaped profiles characteristic of non-exchanging interstitials, with sequestration under those conditions dominated by extended defects.

1. Differential equations for defect reaction and diffusion

Reaction and diffusion behaviors were embodied in continuum equations taking the general form,

$$\frac{\partial C_j}{\partial t} = -\frac{\partial J_j}{\partial x} + G_j, \quad (1)$$

where x and t represent the spatial and temporal coordinates, C_j is the concentration, J_j is the flux and G_j is the net generation rate of interstitial isotope j, respectively. The flux obeys Fickian diffusion for each mobile species with site-hopping diffusivity D_j. The G_j term contains a series of elementary-rate expressions for sequestration and emission in the bulk. The computations assumed a dominant charge state of +4 for Ti_i[10–12] and −2 for O_i.[3,5] In line with prior work, the concentration of O_i was assumed to be in chemical (though not isotopic) equilibrium. However, in light of evidence for non-equilibrium behavior of Ti from previous work[5,8] with small amounts of foreign adsorbate, this assumption was relaxed slightly to quasi-steady state for Ti_i.

Despite the fact that the Ti was not quite in chemical equilibrium in the experiments, approach to equilibrium was likely to be sufficiently close to merit the use of a thermodynamic framework to quantify the total concentration of Ti_i. The computed enthalpy and entropy of formation may not match the true values exactly, but they are likely to be close and thereby offer a useful point of comparison with literature values. The calculations followed the convention of reference[5] to express the total concentration of Ti_i ($C_{Ti,tot}$) as

$$C_{Ti,tot} = C_{Ti,lat}\exp\left(\frac{\Delta S_{f,Ti}}{k_B}\right)\exp\left(-\frac{\Delta H_{f,Ti}}{k_B T}\right)P_{O_2}{}^{-1}\left(\frac{n}{N_c}\right)^{-4}, \quad (2)$$

which describes a function of the standard enthalpy (ΔH_f) and entropy (ΔS_f) of formation, the electron concentration n, and the oxygen partial pressure P_{O_2}. N_C denotes the effective density of states in the conduction band, and T and k_B respectively denote temperature and Boltzmann's constant. $C_{Ti,lat}$ represents the Ti concentration in lattice sites. In this convention, ΔH_f and ΔS_f are defined for Ti_i^{4+} in a hypothetical state wherein the Fermi level E_{Fermi} is located at the valence band maximum. Any Fermi level dependence of the interstitial concentration is contained within the term (n/N_c). The mass action law relates the concentration of n and p according to:

$$np = N_V N_C \exp\left(-\frac{E_g}{k_B T}\right) \quad (3)$$

where E_g is the band gap of rutile and N_V (the effective density of states in the valence band) and N_C vary with temperature.

As the formation enthalpy and entropy for $C_{Ti,tot}$ are model outputs rather than inputs, computation of $C_{Ti,tot}$ ultimately began with the electroneutrality condition for the solid, whereby the sum of charges from donors, acceptors and free carriers must sum to zero. For TiO_2, which is well known to be n-type, the majority donor concentration was computed as indicated below. The electron concentration n was computed from this donor concentration, and the hole concentration p was be calculated through the law of mass action for charge carriers with the known band gap and effective densities of states for TiO_2. The band gap E_g was estimated by the simplified Varshni equation:

$$E_G = E_{0K} - \beta T, \quad (4)$$

where E_{0K} = 3.06 eV and β = 0.00088 eV K^{-1}.[13–15]

Electroneutrality requires that the majority carrier concentration equal the majority donor or acceptor concentration in its primary ionization state, which in the present case leads to

$$n \approx 4C_{Ti,tot}. \quad (5)$$

Five isotopes comprise natural-abundance titanium: ^{48}Ti(73.72%), ^{46}Ti(8.25%), ^{47}Ti(7.44%), ^{49}Ti(5.41%) and ^{50}Ti(5.18%). The total concentration of Ti in the lattice is

$$C_{Ti,tot} = C_{48} + C_{46} + C_{47} + C_{49} + C_{50} = 3.19 \times 10^{22}\ cm^{-3}, \quad (6)$$

where the total lattice titanium concentration remains the same throughout the experiment. For computational efficiency, all non-label Ti isotopes (^{48}Ti, ^{47}Ti, ^{49}Ti, and ^{50}Ti) incorporated into a single aggregate concentration variable.

The flux J for each mobile isotope was assumed to obey Fick's laws of diffusion, with the hopping diffusivity D_{Ti} for $\mathrm{Ti_i}$ represented by the expression,

$$D_{\mathrm{Ti}} = g\ell^2\Gamma. \quad (7)$$

In eqn (7), g denotes a geometric factor that equals 1/6 in three dimensions, ℓ is the hop length which is equivalent to a lattice spacing and Γ is the jump rate that is expressed by,

$$\Gamma = \nu \exp\left(\frac{\Delta S_{\mathrm{diff,Ti}}}{k_{\mathrm{B}}}\right) \exp\left(-\frac{E_{\mathrm{diff,Ti}}}{k_{\mathrm{B}}T}\right). \quad (8)$$

Combining eqn (7) and (8), $D_{\mathrm{M,Ti}}$ can be expressed as,

$$D_{\mathrm{Ti}} = D_{0,\mathrm{Ti}} \exp\left(-\frac{E_{\mathrm{diff,Ti}}}{k_{\mathrm{B}}T}\right), \quad (9)$$

where D_0 is the pre-exponential factor,

$$D_{0,\mathrm{Ti}} = \frac{1}{6}\nu l^2 \exp\left(\frac{\Delta S_{\mathrm{diff,Ti}}}{k_{\mathrm{B}}}\right)$$

In rutile, Ti and O interstitials exchange with the edges[16,17] of platelets and crystallographic shear planes in a 1 : 2 stoichiometric ratio. Accretion is diffusion-limited, and emission is thermally activated. Molecular dynamic simulations suggest that extended defects interact more strongly with negative ions such as $\mathrm{O_i}^{2-}$[17] than with positive ions, so association of $\mathrm{Ti_i}^{4+}$ constitutes the rate-limiting step for accretion.

As an approximation, all extended defects in the bulk were assumed to have the same properties with respect to exchange kinetics with $\mathrm{Ti_i}$. The stoichiometric equations for exchange could then be written as:

$$\mathrm{Ti_i} + E \underset{k_{\mathrm{dssc,Ti}}}{\overset{k_{\mathrm{assc,Ti}}}{\longleftrightarrow}} E, \quad (10)$$

with extended defects of all kinds lumped into a single concentration variable [E]. The simulations described the forward accretion reaction with a conventional diffusion-limited reaction expression.

Emission of $\mathrm{Ti_i}$ as assumed to follow first order kinetics in [E] with dissociation rate constant, k_{dssc},

$$k_{\mathrm{dssc}} = A_{\mathrm{dssc}} \exp\left(-\frac{E_{\mathrm{dssc}}}{k_{\mathrm{B}}T}\right) \quad (11)$$

where A_{dssc} is the pre-exponential factor and E_{dssc} is the activation energy. To maintain extended defect stoichiometry, the emission expression for Ti was multiplied by a factor of two to yield the rate of $\mathrm{O_i}$.

Accretion of Ti was also assumed to follow first order kinetics in [E] and in C_{Ti}, with a standard diffusion limited rate constant k_{assc}:

$$k_{\mathrm{assc}} = 4\pi a_{\mathrm{E}} D_{\mathrm{Ti}}. \quad (12)$$

D_{Ti} is the diffusivity for $\mathrm{Ti_i}$ and a_{E} is the capture radius set to 2×10^{-8} cm. This radius represents an approximation, as the actual capture radius depends on several factors including the extended defect type as well as the charge state and identity of the atoms involved.[18] To maintain extended defect stoichiometry, the accretion expression for Ti was multiplied by a factor of two to yield the rate of $\mathrm{O_i}$.

Two distinct spatial regions characterize the concentration of extended defects in the presence of gaseous Ti:[8] a skin region extending about 20 nm from the surface, and a deep bulk region further down. Experimental profiles for isotopic Ti (and O) exhibit exponential shapes when plotted in suitable normalized form, as shown in Fig. 3. Because the skin region grades smoothly into the deep-bulk region, a curvature parameter κ was computed point by point to delineate the boundary between the regions.[8] In the skin region, the shapes often exhibit curvature that is convex upward in Fig. 3, indicative of the nucleation and growth of extended defects. Although the same rate expressions and parameters for exchange with extended defects were employed throughout the solid, [E] was treated differently in the skin and deep bulk regions.

In the deep bulk, the extended defects undergo ripening in size and concentration during the isotopic exposure. Their concentration varies with temperature due to the conventional ripening processes that extended defects often undergo.[19–23] The rate of such ripening in $\mathrm{TiO_2}$ depends upon the availability of $\mathrm{Ti_i}$, as the concentration of $\mathrm{O_i}$ appears to be essentially in chemical equilibrium[4] while the concentration of $\mathrm{Ti_i}$ slowly evolves.

To account for ripening mechanism of the extended defects that were already present at the start of isotopic exposure (after the initial annealing in natural abundance $\mathrm{O_2}$), [E] was estimated in the deep bulk region through a simplified Gibbs-Thomson expression[24–26] for Ostwald ripening:

$$\exp(\Omega), \quad (13)$$

where Ω is a parameter that depends on a ripening enthalpy $\Delta H_{\mathrm{ripen}}$ according to:

$$\Omega = \frac{2\Delta H_{\mathrm{ripen}}}{k_{\mathrm{B}}T} \quad (14)$$

that was adapted from the experimental work of Madras *et al.*[24,26,27] The bulk extended defect concentration then becomes,

$$[\mathrm{E}] = \exp(\Omega) C_{\mathrm{E}}, \quad (15)$$

where C_{E} is a baseline concentration of the extended defects that was determined to be 1×10^{16} $\mathrm{cm^{-3}}$ from manual fitting of the Ti profiles at 650 °C and an oxygen pressure of 5×10^{-6} Torr.

In the skin region, an additional contribution to [E] was included due to nucleation and growth. The spatial variation of this contribution undoubtedly varied not only with temperature but also with time during the isotopic exposure. Because explicit temporal dependence in the rate expressions presents a difficult mathematical problem that lies beyond the capabilities of the numerical differential equation solver employed here, and because the isotopic exposure time was always the same in the experiments, the simulations included the temporal dependence only implicitly and phenomenologically through the temperature dependence. Based upon visual inspection of

the Ti and O profile shapes, the additional contribution to [E] was assumed to have a Gaussian functional form on depth x from the surface:

$$f(x) = \alpha \exp\left(-\frac{x^2}{2c^2}\right) \quad (16)$$

where c describes the characteristic width of the skin region and α describes the amplitude. The quantity c was set equal to 20 nm for Ti based upon manual fittings of Ti experimental profiles at 5×10^{-6} Torr. The functional form of α originates from an expression adapted from Chao *et al.*[28] to quantify the concentration of dislocation loops in silicon, and obeys:

$$\alpha = 4\pi\left(\frac{r_E}{r_{latt}}\right)^2 (D_{Ti} + D_O) \exp\left(-\frac{\Delta H_{growth}}{k_B T}\right) q_c, \quad (17)$$

where r_E denotes the radius of a spherical extended defect and r_{latt} denotes the interatomic spacing of the lattice. ΔH_{growth} represents the activation enthalpy for extended defect growth, and q_c is a phenomenological fitting parameter. The average radius r_E was estimated to be about 10 nm based upon existing literature for platelets in TiO_2, and r_{latt} equals 1.77×10^{-8} cm. The constant q_c was determined to be 1×10^6 based upon manual fitting of the Ti and O profiles at 5×10^{-6} Torr. Eqn (17) differs slightly from that of Chao *et al.*[28] in order to represent extended defects as a spheres rather than tori in accord with the literature for rutile TiO_2.[19] D_{Ti} dominates D_O in eqn (17), as extended defect growth is limited by Ti diffusion.

Fig. 2 shows an example of [E] *vs.* depth in the skin region for a typical set of conditions employed in the simulations. The additional contribution to [E] exceeds the baseline contribution from the deep bulk by a large factor – about 10^3 in the case of Fig. 2.

2. Boundary and initial conditions

The initial conditions for C_j assumed that each isotope was at its natural-abundance equilibrium value throughout the solid. For boundary conditions deep within the solid, the concentrations C_j were assumed to remain at their natural abundance values with no spatial variation. Mathematically, these conditions were implemented by $\partial C_j/\partial x = 0$ as $x \to \infty$. The corresponding boundary conditions at the surface incorporate kinetic expressions for defect injection and annihilation. The surface conditions obey the form:

$$-D_j \left.\frac{\partial C_j}{\partial x}\right|_{x=0} = r_{inj,j} - r_{ann,j}, \quad (18)$$

where $r_{inj,j}$ and $r_{ann,j}$ respectively denote the elementary-step injection and annihilation rates. The rates of adsorption and desorption from the gas were assumed to be much faster than that of interstitial annihilation and injection. This assumption has been justified elsewhere for oxygen.[5] For Ti, separate control experiments involving epitaxial film TiO_2 film growth of measureable thicknesses at much higher O_2 pressures showed that the r_{inj} calculated in the sections below remained far less than the incident flux of Ti from the gas phase.

The principle of detailed balance requires that the surface injection sites be identical to the annihilation sites, and we assume those sites contain a well-defined concentration θ of injectable Ti. Annihilation and injection kinetics were described by direct analogy to adsorption and desorption of gaseous species according to first-order Langmuir-type expressions.[21] The annihilation/injection sites for Ti_i (all isotopes) have a fractional coverage θ_{Ti}. The injection rate follows first-order kinetics:

$$r_{inj,Ti} = k_{inj,Ti} n_{sat,Ti} \theta_{Ti}. \quad (19)$$

where $k_{inj,Ti}$ denotes the injection rate constant for Ti_i and n_{satTi} is the maximum concentration of injection sites per unit area under the experimental conditions. Upon initiation of isotopic exposure, the relative contribution of each isotope to θ_{Ti} was assumed to reflect that of the incoming flux from the gas phase, meaning that is θ_{46Ti} comprises 76.4% of the total. The injection rate constant was expressed as:

$$k_{inj} = \nu_{inj} \exp\left(-\frac{E_{inj}}{k_B T}\right), \quad (20)$$

where E_{inj} is the activation energy and ν_{inj} is the pre-exponential factor with a value assumed to be a typical value of 1.0×10^{13} s^{-1}.

The annihilation rate for Ti_i was expressed as,

$$r_{ann,Ti} = \frac{3 D_{Ti} S_0}{\ell_{Ti}} \Theta_{sat,Ti} (1 - \theta_{Ti}) C_{Ti_{i,x=0}}, \quad (21)$$

where ℓ_{Ti} is the diffusive site-to-site hopping length for Ti_i and S_0 denotes a constant zero-coverage sticking probability. The fractional concentration of injectable Ti was scaled to a theoretical maximum value $n_{satmaxTi}$, which in principle can vary with the particular surface reconstruction present and poisoning by foreign adsorbates. Such effects were incorporated through the quantity

$$\Theta_{sat,Ti} = \frac{n_{sat,Ti}}{n_{satmax,Ti}}. \quad (22)$$

Coverage calculations made use of the quasi-steady state conditions at the surface, which require that the injection rate of Ti_i (summed over all isotopes) equals the annihilation rate:

$$n_{sat,Ti} \frac{\partial \theta_{Ti}}{\partial t} = D_{Ti} \left.\frac{\partial C_{Ti,tot}}{\partial x}\right|_{x=0} = -r_{inj} + r_{ann} = 0. \quad (23)$$

This leads to the following expression for θ_{Ti}:

$$\theta_{Ti} = \frac{3 D_{Ti} S_0 C_{Ti,tot(x=0)}}{n_{sat,max} l \nu_{inj} e^{-\frac{E_{inj}}{k_B T}} + 3 D_{Ti} S_0 C_{Ti,tot(x=0)}}. \quad (24)$$

3. Parameter estimation and confidence intervals

Activation energies, pre-exponential factors, and other parameters embedded within the system of equations represented by eqn (1) were determined *via* the least squares technique of weighted sum of square errors (WSSE). Application of this approach to oxygen in TiO_2 has been described in detail elsewhere,[5]

and relies upon iterative solution of the coupled system of eqn (1) for each interstitial defect species using the FLOOPS simulator.[29] The resulting simulations yield concentration depth profiles of the isotopically labeled elements diffusion profiles $C_{exp}(x)$. The difference between the simulated and experimental profiles, $C_{sim}(x) - C_{exp}(x)$, is computed for a discrete set of depths x for each profile and the WSSE objective function is then minimized as the constituent parameters are varied systematically in small increments. Only parameters with significant sensitivity coefficients (from a separate sensitivity analysis) were adjusted. Separate objective functions were defined for O_i and Ti_i that were minimized in multiple sequential iterations. Iterations were terminated when the objective functions for both O and Ti changed by less than a tolerance of 0.1%. Confidence intervals at the 67% level were computed as described elsewhere.[5] After the procedure was finished, the results for O_i remained fairly close to those previously published[5] for the large majority parameters where direct correspondence could be established.

Several initial parameters were determined from quantum calculations in the literature.[9,30,31] Values for the enthalpy and entropy of formation for Ti_i in rutile TiO_2 were gleaned from experimental literature,[10,11,15,30,32–35] with using maximum likelihood estimation employed to obtain aggregated averages from multiple reports.[9] Calculation of N_C and N_V employed effective masses of electrons and holes given in the literature.[36–42] For emission from extended defects, a value of 3.2 eV was based upon the analogous process for self-interstitials from interstitial clusters in silicon,[18] which is as a loosely similar semiconductor system. For oxygen, initial parameters were mostly taken from a previous microkinetic model.[5]

Results

Table 1 shows parameter estimates and confidence intervals for the optimal Ti_i WSSE values. The final values do not change significantly from the initial value except those for ΔH_{growth} and ΔH_{ripen} decrease by ~70%. Fig. 1 shows representative experimental and simulated profiles for ^{46}Ti at $P_{O_2} = 5 \times 10^{-6}$ Torr. The simulated profiles replicate the experimental data fairly accurately in the deep bulk, but exhibit more convexity in the skin region.

Table 1 Initial and final parameters for Ti_i

Parameter	Eq.	Initial value	WSSE estimate value
ΔH_f	18	10.67 eV	10.1 ± 0.2 eV
ΔS_f	18	$2.38 \times 10^{-3} k_B$	$(2.15 \pm 0.1) \times 10^{-3} k_B$
ΔH_{growth}	24	0.7 eV	0.15 ± 0.05 eV
ΔH_{ripen}	27	0.7 eV	0.20 ± 0.05 eV
$E_{diff,M}$	49	1.0 eV	0.5 ± 0.02 eV
$D_{o,M}$	49	1.0×10^{-2} cm^2 s^{-1}	$(5.0 \pm 0.2) \times 10^{-3}$ cm^2 s^{-1}
ν_{inj}	30	1.0×10^{13} s^{-1}	$(1.0 \pm 0.1) \times 10^{13}$ s^{-1}
E_{inj}	30	0.5 eV	0.55 ± 0.01 eV
A_{dsscTi}	46	1.0×10^{13} s^{-1}	$(1.0 \pm 0.1) \times 10^{13}$ s^{-1}
E_{dsscTi}	46	3.2 eV	3.3 ± 0.4 eV
S	34	1×10^{-6}	$(5.0 \pm 0.1) \times 10^{7}$ cm^{-2}
$N_{sat,Ti}$	33	1×10^{14} cm^{-2}	
$N_{satmax,Ti}$	33	2.6×10^{14} cm^{-2}	2.6×10^{14} cm^{-2}

$S \times n_{sat,Ti}$ cannot be deconvolved.

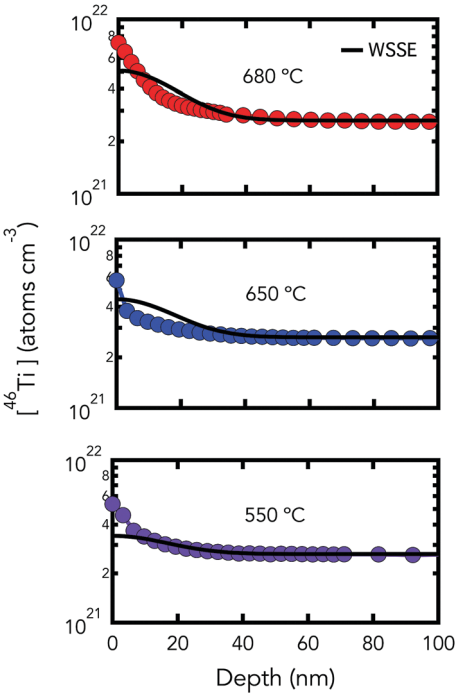

Fig. 1 Examples of isotopic Ti diffusion profiles for Ti-flux surface simulated based on WSSE optimized parameters (black lines) compared to corresponding experimental profiles (symbols). Oxygen pressure was 5×10^{-6} Torr.

An analytical model can be applied to each experimental profile[43,44] to yield the net surface flux F of the injected marker, its mean diffusion length λ, and the effective diffusivity D_{eff} characterizing the profiles (distinguished from the hopping diffusivity D_{Ti} of the mobile intermediate). The composite parameter D_{eff} is given by

$$D_{eff} = \frac{F\lambda}{\left[C^{T}_{S,t_0} - C^{18}_{S,t_0}\right]}. \quad (25)$$

This analytical approach aggregates the profile data differently from the WSSE method. WSSE considers all the profiles simultaneously in a global way to obtain fundamental quantities such as E_{inj} and $E_{diff,M}$, with heavier weighting given to values of C_S^{18} that have smaller standard deviations (and are typically large). Composite parameters such as F and λ can be then calculated by relations such as eqn (18) and (for sequestration by extended defects):

$$\lambda = \sqrt{\frac{1}{4\pi r_E [E]}}. \quad (26)$$

In contrast, the analytical approach yields F, λ and D_{eff} on a profile-by-profile basis, with all data points within the profile given the same weight in a least-squares fit. In turn, the temperature dependencies represented by parameters such as E_F and E_λ come from least-squares Arrhenius fits of the profile-by-profile numbers. Because of these methodological differences, the WSSE and analytical results for the temperature and pressure dependencies of F, λ and D_{eff} are likely to differ.

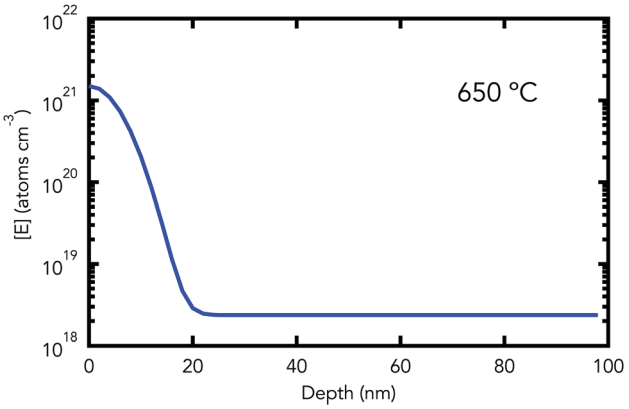

Fig. 2 Graphical depiction of [E] as a function of depth at P_{O_2} of 5.0×10^{-6} Torr.

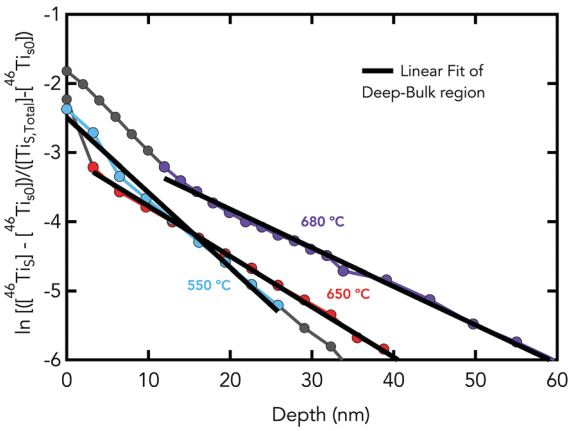

Fig. 3 ^{46}Ti diffusion profiles on a semilogarithmic scale. The characteristic diffusion length, λ, can be determined from the slope of the linear fit in the deep-bulk region.

Fig. 4 compares in Arrhenius form key results for D_{eff}, F and λ from the microkinetic and analytical approaches. The values of D_{eff} and λ are shown in the deep-bulk region. The results for λ match quite closely between the two methods, but microkinetic approach yields a much stronger temperature dependence for D_{eff} and F. The plots cross each other approximately where the density of data points is highest. Table 2 tabulates the temperature dependences of these quantities through their effective activation energies E_{F}, E_{λ} and E_{diff}. Although E_{λ} matches for the two approaches, E_{diff} and E_{F} from the microkinetic approach exceeds their analytical counterparts by nearly 2 eV.

Fig. 5 shows the coverage of injectable Ti in the temperature range of 700 K to 1200 K, which includes the range 820–1030 K of the experiments. The coverage increases with temperature, although the slope first increases slightly in a pressure-dependent way and then decreases. At the high end of the temperature range, the effective pressure of Ti exerts no effect on θ_{Ti}. At the low end, θ_{Ti} increases rather weakly with pressure. The transition between the two regimes fortuitously occurs within the experimental temperature range.

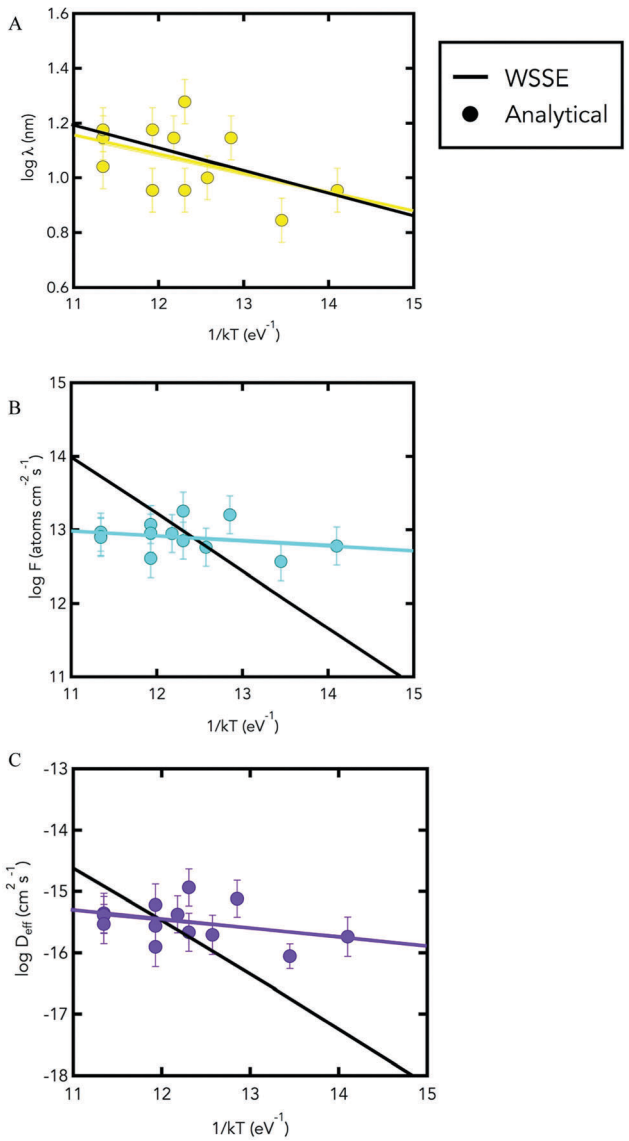

Fig. 4 Ti$_i$ diffusion Arrhenius plots of (A) characteristic diffusion length, λ, (B) net injection flux, F, and (C) effective diffusivity, D_{eff}, for the analytical and WSSE method to analyzing isotopic diffusion profiles. Analytical results have discrete data points for each profile (symbols) and a least-squares fit (line), the simulated WSSE results are represented by the black line.

Table 2 Ti$_i$ activation energies for F, λ and D_{eff} calculated using the analytical and WSSE method

	Activation energy	Clean (eV)
Analytical	E_{λ}	0.18 ± 0.08
	E_{F}	0.17 ± 0.10
	$E_{D_{\text{eff}}}$	0.35 ± 0.25
WSSE	E_{λ}	0.22 ± 0.02
	E_{F}	2.08 ± 0.04
	$E_{D_{\text{eff}}}$	2.30 ± 0.04

Fig. 6 shows the predicted point defect and carrier concentrations in the deep bulk region as a function of temperature at the experimental pressure $P_{O_2} = 5.0 \times 10^{-6}$ Torr and as a

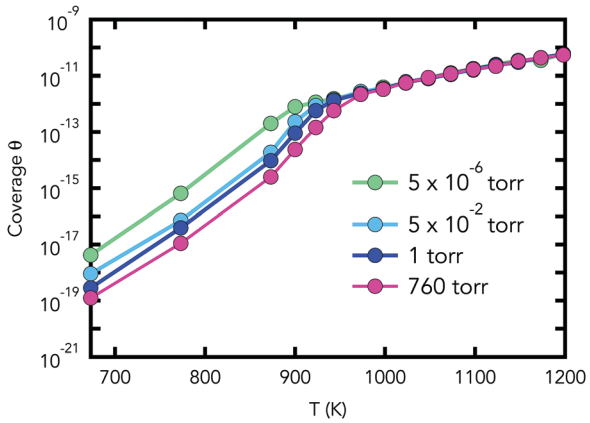

Fig. 5 Coverage of injectable Ti as a function of temperature and oxygen pressure. The experimental temperature range was 820–1030 K, with an approximate effective pressure of Ti on the order of 10^{-7} Torr.

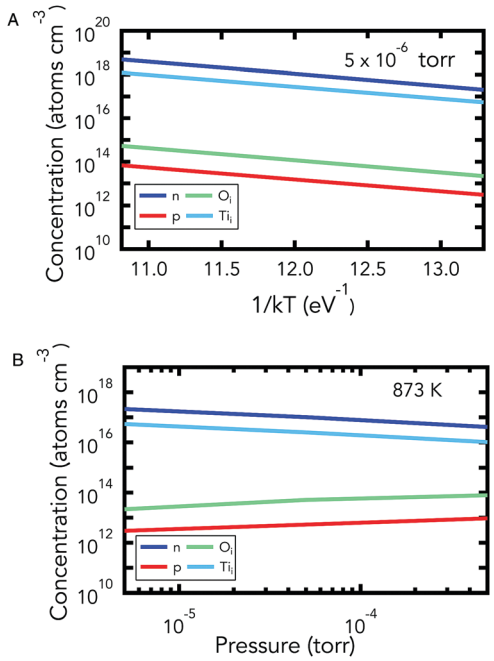

Fig. 6 (A) Equilibrium defect and carrier concentration in rutile TiO_2 at $P_{O_2} = 5 \times 10^{-6}$ Torr. (B) Equilibrium defect and carrier concentrations in rutile TiO_2 at 873 K as a function of pressure between $P_{O_2} = 5 \times 10^{-4}$ and 5×10^{-6} Torr.

function of oxygen pressure at 873 K. All point defect and carrier concentrations rise in Arrhenius fashion as temperature increases. The concentration of Ti_i exceeds that of O_i by over three orders of magnitude, and accordingly the rutile is strongly n-type. As the oxygen pressure increases, the concentration of holes and O_i increases while the concentration of electrons and Ti_i decreases.

Fig. 7 shows the temperature dependence of the net injected fluxes of ^{46}Ti and the aggregated other isotopes in Arrhenius form. This figure also shows the elementary-step components r_{inj} and r_{ann} for the isotopic label. The net injection flux of ^{46}Ti exceeds that of the other aggregated isotopes, in accord with the

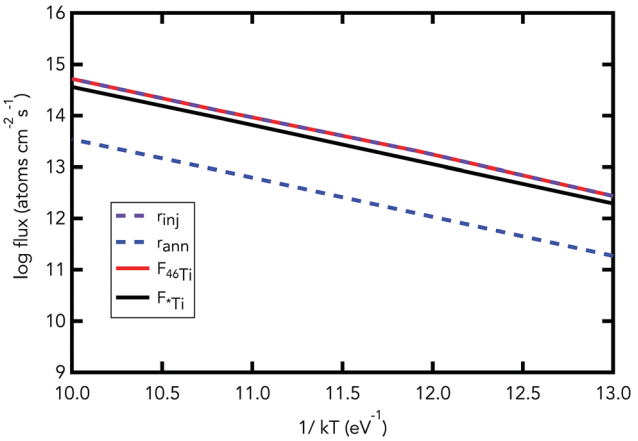

Fig. 7 Net fluxes of $^{46}Ti_i$ and $*Ti_i$ (all other isotopes of Ti) at $PO_2 = 5 \times 10^{-6}$ Torr and the elementary-step components of the net injection rate for $^{46}Ti_i$.

isotopic enrichment of the gas phase. The net isotopic injection flux reflects mainly r_{inj} rather than a small difference between the constituent injection and annihilation rates. Elementary-step injection dominates annihilation by about an order of magnitude. All the flux magnitudes are quite large, however, with F near one monolayer per second at the upper end of the temperature range.

As the thermodynamic parameters for a charged defect vary with E_{Fermi}, it is useful to compute a formation enthalpy ΔH_f^* for Ti_i at the value of E_{Fermi} that exists under the experimental conditions. Direct manipulation of thermodynamic expressions for Ti_i shows that

$$\Delta H_f^* = \Delta H_f - 4E_{Fermi}. \quad (27)$$

For the value of E_{Fermi} of about 2.4 eV at 773 K that prevails in the experiments, ΔH_f^* is roughly 3.1 eV. E_{Fermi} decreases somewhat with increasing pressure and temperature, which thereby induces a corresponding increase in ΔH_f^*.

Discussion

1. O_i and Ti_i thermodynamic quantities

The microkinetic value of ΔH_f for Ti_i of 10.1 ± 0.2 eV falls within the range of values between 10.13–11.98 eV already published for rutile.[11,45–47] Comparable values computed by first-principles density functional theory (DFT) lie about ~20% higher at 11.59 eV,[34] 12.18 eV[10] and 12.13 eV.[30] The reason for the difference is unclear. The microkinetic value of ΔS_f is $(2.15 \pm 0.01) \times 10^{-3} k_B$, which is very close to experimental reports of $2.47 \times 10^{-3} k_B$[45] and $2.29 \times 10^{-3} k_B$.[46] All these numbers are quite small, and point to negligible contributions of vibrational or ionization contributions in the formation process. The effective formation enthalpy $\Delta H_{f,Ti}^*$ for Ti_i^{4+} is 3.1 eV, where,

$$\Delta H_f^* = \Delta H_f + (-4)E_{Fermi}. \quad (28)$$

The close resemblance of this value to the barrier (3.3 eV) for Ti_i from extended defects may not be coincidental; as the atomic

bonding within an extended defect is broadly similar to the that within the thermodynamic reference state for Ti_i.

2. Ti_i diffusion and sequestration in rutile TiO_2

Table 1 shows a value of 0.50 eV for the activation energy for Ti_i site-to-site hopping. The corresponding value from DFT is 0.37 eV.[30] Both numbers fall below the 0.65 eV for O_i, and follow a similar ordering revealed by DFT studies of O_i and Zn_i in ZnO.[48–50] The barrier for Ti_i are also modest compared to 0.72 eV for self-interstitials in Si.[51] Despite the lower hopping energy for Ti than O, D_{Ti} remains lower than D_O because the prefactor for D_{Ti} is 16 times less.

The barrier for Ti_i emission from extended defects is 3.3 eV. To our knowledge the literature reports no directly comparable number. One rough analog is the emission of Si_i and B_i from extended defects (clusters, {311} loops, dislocations) in silicon,[18,52] with an activation energy between 3.5 and 3.7 eV. This range lies close to the value for TiO_2.

The strong temperature dependence of D_{eff} and F in the microkinetic approach compared to the analytical approach deserves comment. As indicated in ref. 8, the experimental values of F were determined directly from the areas under the entire profiles – including both the skin and deep bulk regions. The overwhelming majority of the injected isotope resides within the skin region. The time-dependent effects of extended defect nucleation and growth are also most pronounced in this region. As described in the computational methods, the simulation platform employed here forces these temporal effects to be subsumed within the effective temperature dependence. That approximation may be too severe. As the computed values of D_{eff} in the deep bulk region contain F as indicated in eqn (26), problems in computing F propagate linearly into D_{eff}.

An additional weakness of the analytical approach also deserves mention. The analytical approach employs a deep-bulk boundary condition of $\partial C_j/\partial x = 0$ as $x \rightarrow \infty$. Yet numerical implementation of this boundary condition requires the establishment of specific values for the Ti_i and O_i steady-state concentrations in the deep bulk. Such establishment tacitly presupposes the existence of a defect disorder model with the appropriate thermodynamic quantities. Yet such a model does not exist for rutile that includes both O_i and Ti_i; that is partly what the microkinetic model seeks to accomplish. Use of the analytical approach as the initial technique for profile correlation requires the *a priori* assumption of deep-bulk concentrations of O_i and Ti_i that are typically independent of both temperature and pressure. The specific value employed in ref. 3–5 and 8 was 1×10^{15} cm^{-3}. This value is crudely approximates the geometric mean of the microkinetic values shown in Fig. 5, but differs by roughly 1–2 orders of magnitude from both. Obviously the microkinetic approach permits the variation of both the O_i and Ti_i concentrations with T and P.

3. Surface kinetics

The WSSE value of 5.0×10^7 cm^{-2} for the composite parameter $n_{sat,Ti}S_0$ lies nearly two orders of magnitude below that reported in ref. 5 and 53 for O_i. As suggested in an earlier publication,[8] presence of Ti in the gas phase induces a surface reconstruction from (1×1) to Ti-rich (1×2) periodicity whose changed atomic geometry could easily propagate into both $n_{sat,Ti}$ and S_0. This reconstruction appears to increase either or both of the number and efficiency of O_i injection sites, and net injection rates for Ti_i injection are close to those for O_i. It seems plausible that $n_{sat,Ti}$ is comparable to the corresponding value for O_i, although injection sites occasionally compose only a small fraction of the surface atom density for a given element.[6] Hence, it seems likely, though not certain, that the small value of $n_{sat,Ti}S_0$ originates from a small value of S_0 rather than $n_{sat,Ti}$.

The surface injection barrier of Ti_i is 0.55 eV. This value agrees rather well with the values of 0.44 eV[54] from scanning transmission microscopy and 0.47 eV[9] from DFT. This agreement supports the important point that the microkinetic approach yields good estimates of injection barriers even when the T dependence of F suffers the problems discussed above. The modest barrier undoubtedly facilitates the growth of the near-surface extended defects observed in the presence of gaseous Ti.[19,20] Curiously, the injection barrier is only slightly greater than the site-to-site hopping barrier in the bulk. This behavior contrasts markedly with O_i injection of Zn-terminated ZnO(0001), where the DFT-computed barrier of 1.7 eV considerably exceeds the corresponding hopping barrier of 0.35 eV.[7] The key geometries involved in Ti_i injection into TiO_2 involve unusual behavior, however. DFT calculations show that Ti adatoms on the surface distort the configuration of nearby O atoms[54] so severely that Ti_i in the bulk is actually more stable than Ti adatoms by 0.5 eV or more.[30] This counterintuitive behavior undoubtedly facilitates injection of Ti by the surface. Although these calculations involved the (1×1) rather than the (1×2) reconstruction believed to prevail in the present experiments, a related facilitation probably occurs.

4. Defect coverage

Given the evaporation source for Ti employed in the experiments, the effective pressure of Ti at the surface is not known. However, separate experiments involving the growth of isotopic heterostructures of TiO_2[53] employed the same source, and established a minimum value for the Ti flux at $\sim 10^{12}$ atom per cm^2 s^{-1}. Although the sticking probability of the adsorbing Ti species is unknown, assumption of a maximum value of unity leads to a minimum effective value for P_{Ti} of $\sim 10^{-7}$ Torr. The behavior of θ_{Ti} in Fig. 4 exhibits two striking characteristics: the increase as T rises and the low absolute values. In the temperature range of the experiments, θ_{Ti} rises modestly and exhibits only a weak pressure dependence.

The upward trend in θ_{Ti} runs opposite to the analogous case of gaseous adsorbates, for which coverage generally decreases with increasing temperature. Such behavior in θ has been observed for O injection into ZnO[55] and represents a qualitative difference from surface-gas equilibrium. The difference originates primarily from the existence in the solid case of temperature-dependent terms for defect hopping and charging. The effects of solid hopping enter through E_{diff}, and those of charging manifest through $\left(\frac{p}{N_V}\right)^{-2}$ and its multiplying factor that contains ΔH. These terms have no counterparts in

surface-gas equilibrium. Furthermore, although defect annihilation at a surface bears some resemblance to gas adsorption, the diffusional hop that leads directly to an annihilation event necessarily incorporates significant thermal activation. In contrast, barriers to gas adsorption are typically much smaller. Only defect injection (through E_{inj}) has a direct counterpart to gas desorption (through the desorption barrier). The increase in θ_{Ti} differs from that for θ_O[5] and does not necessarily generalize to other metal oxides, as the numerical values of the parameters contributing to eqn (25) may conspire in very different ways.

The values of θ_{Ti} lie in the range of only a few thousand injectable atoms per square centimeter. Such a value is unphysically low, and would require injection rates of a few atoms per picosecond at each site to reach the measured values. Outside the experimental range, values of θ_{Ti} drop below 1 cm^{-2} at 775–850 K depending upon pressure, and do not reach unity until $T > 10^5$ K. Such behavior points to problems with either the kinetic expressions employed for injection and annihilation or assumptions about certain constituent numerical parameters.

The problem probably stems from the assumption that the pre-exponential factor for injection is roughly 10^{13} s^{-1}. As indicated above, the barrier for injection of Ti_i is unusually low. In gas desorption, systems with unusually low desorption barriers often have correspondingly low pre-exponential factors that compensate.[56,57] Examples include $Ga(C_2H_5)_3$ desorbing from GaAs(110)[58] and $GeCl_2$ desorbing from Ge(100) and (111),[59] where the prefactors range from 10^5 to 10^7 s^{-1} with corresponding barriers of 0.8–1.1 eV. If such compensation characterizes defect injection, then the value of 10^{13} s^{-1} assumed for ν_{inj} is much too high and may need to be lowered by a factor of 10^6 or more. This change would increase the computed values of θ_{Ti} by exactly the same factor. For example, with ν_{inj} assumed to be 10^6–10^7 s^{-1}, θ_{Ti} would rise to 10^{-2}–10^{-3} in the experimental range. The apparently unphysical behavior would largely disappear.

Conclusion

Although microkinetic modeling of networks for the diffusion and reaction of point defects in elemental semiconductors such as silicon has been practiced for several decades, corresponding efforts in oxide semiconductors – especially with surfaces nearby – remain in their infancy. The present work for Ti_i in TiO_2 represents the first such attempt for a cation defect. The resulting microkinetic estimates of barriers for injection and site hopping lie gratifyingly close to corresponding numbers in the literature, and the barrier for Ti_i emission resembles that for the closest available system in the literature. Such results offer confidence that the microkinetic approach holds promise for cations in other metal oxide semiconductors. The counter-intuitive behavior predicted for injectable cation coverage, and the suggested change in cation annihilation rate due to surface reconstruction, point to aspects of the system that might be examined to accomplish defect manipulation intentionally. Microkinetic models have long provided a useful basis for such manipulation in silicon. The suggested anomaly in the pre-exponential factor for injection points to a curiosity in the fundamental chemistry of defect injection that may resemble analogous phenomena in gas desorption.

However, the results described here also highlight important challenges for realizing that promise. Isotopic heterojunctions involving the metal cation are difficult and costly to fabricate for metal oxides, so the primary experimental data will commonly involve exposure to gaseous isotopic label as in the present case. Even with quite modest gas fluxes of the metallic label, time-dependent nucleation and growth of extended defects near the surface greatly complicate the data interpretation and simulation. The present work employed a parameterized and semi-empirical description that was constrained to fold time-dependent effects into effective temperature-dependent input parameters. This constraint degraded the ability of the model to adequately reproduce the net injection flux. A differential equation solver of higher sophistication, or a Monte Carlo approach to simulating the governing equations, could perhaps remove the mathematical difficulty. Yet incorporation of reliable nucleation and growth kinetics would remain challenging, as such kinetics are typically unknown.

Conflicts of interest

There are no conflicts to declare.

Acknowledgements

This work was partially supported by the National Science Foundation (DMR 13-06822 and 17-09327). SIMS was performed at the Center for Microanalysis of Materials at the University of Illinois at Urbana-Champaign.

References

1 E. G. Seebauer, K. Dev, M. Y. L. Jung, R. Vaidyanathan, C. T. M. Kwok, J. W. Ager, E. E. Haller and R. D. Braatz, *Phys. Rev. Lett.*, 2006, **97**, 1.
2 X. Zhang, M. Yu, C. T. M. Kwok, R. Vaidyanathan, R. D. Braatz and E. G. Seebauer, *Phys. Rev. B: Condens. Matter Mater. Phys.*, 2006, **74**, 235301.
3 P. Gorai, A. G. Hollister, K. Pangan-Okimoto and E. G. Seebauer, *Appl. Phys. Lett.*, 2014, **104**, 191602.
4 A. G. Hollister, P. Gorai and E. G. Seebauer, *Appl. Phys. Lett.*, 2013, **102**, 8.
5 K. M. Pangan-Okimoto, P. Gorai, A. G. Hollister and E. G. Seebauer, *J. Phys. Chem. C*, 2015, **119**, 9955.
6 M. Li and E. Seebauer, *J. Phys. Chem. C*, 2016, **120**, 23675.
7 P. Gorai, E. Ertekin and E. Seebauer, *Appl. Phys. Lett.*, 2016, **108**, 241603.
8 K. Gilliard and E. G. Seebauer, *J. Phys.: Condens. Matter*, 2017, **29**, 1.

9 P. a Mulheran, M. Nolan, C. S. Browne, M. Basham, E. Sanville and R. a Bennett, *Phys. Chem. Chem. Phys.*, 2010, **12**, 9763.
10 X. Li, M. W. Finnis, J. He, R. K. Behera, S. R. Phillpot, S. B. Sinnott and E. C. Dickey, *Acta Mater.*, 2009, **57**, 5882.
11 W. M. Blumenthal, R. N. Baukus and J. Hirthe, *J. Electrochem. Soc.*, 1967, **114**, 172.
12 K. Hoshino, N. L. Peterson and C. L. Wiley, *J. Phys. Chem. Solids*, 1985, **46**, 1397.
13 J. F. Baumard and E. Tani, *Phys. Status Solidi*, 1977, **39**, 373.
14 J. Yahia, *Phys. Rev.*, 1963, **130**, 1711.
15 T. Bak, J. Nowotny, M. K. Nowotny and L. R. Sheppard, *J. Aust. Ceram. Soc.*, 2008, **44**, 63.
16 B. P. Uberuaga and X.-M. Bai, *J. Phys.: Condens. Matter*, 2011, **23**, 435004.
17 X. Bai and B. P. Uberuaga, *Philos. Mag.*, 2012, **92**, 1469.
18 R. Gunawan, M. Y. L. Jung, R. D. Braatz and E. G. Seebauer, *J. Electrochem. Soc.*, 2003, **150**, G758.
19 L. A. Bursill, M. G. Blanchin and D. J. Smith, *Proc. R. Soc. London, Ser. A*, 1984, **391**, 373.
20 M. G. Blanchin, L. A. Bursill and D. J. Smith, *Proc. R. Soc. London, Ser. A*, 1984, **391**, 351.
21 A. Claverie, F. Cristiano, B. Colombeau, E. Scheid and B. De Mauduit, *Proc. Int. Conf. Ion Implant. Technol.*, 2002, pp. 538–543.
22 V. Moroz, I. Martin-Bragado, S. Felch, F. Nouri, C. Olsen and K. S. Jones, *J. Vac. Sci. Technol., B: Microelectron. Nanometer Struct.–Process., Meas., Phenom.*, 2008, **26**, 439.
23 P. A. Stolk, H. J. Gossmann, D. J. Eaglesham, D. C. Jacobson, S. Rafferty, G. H. Gilmer, M. Jaraiz, J. M. Poate, H. S. Luftman and T. E. Haynes, *J. Appl. Phys.*, 1997, **81**, 6031.
24 G. Madras and B. J. McCoy, *Chem. Eng. Sci.*, 2002, **57**, 3809.
25 P. W. Voorhees, *J. Stat. Phys.*, 1985, **38**, 231.
26 G. Madras and B. J. McCoy, *J. Chem. Phys.*, 2003, **119**, 1683.
27 G. Madras and B. J. McCoy, *J. Chem. Phys.*, 2001, **115**, 6699.
28 H. S. Chao, P. B. Griffin and J. D. Plummer, *Appl. Phys. Lett.*, 1996, **68**, 3570.
29 M. E. Law and S. M. Cea, *Comput. Mater. Sci.*, 1998, **12**, 289.
30 H. Iddir, S. Öğüt, P. Zapol and N. D. Browning, *Phys. Rev. B: Condens. Matter Mater. Phys.*, 2007, **75**, 2.
31 D. K. Lee and H. I. Yoo, *Solid State Ionics*, 2006, **177**, 1.
32 H. Y. Lee and J. Robertson, *J. Appl. Phys.*, 2013, **113**, 213706.
33 H. Kamisaka and K. Yamashita, *J. Phys. Chem. C*, 2011, **115**, 8265.
34 H. Peng, *Phys. Lett. A*, 2008, **372**, 1527.
35 G. Mattioli, P. Alippi, F. Filippone, R. Caminiti and A. A. Bonapasta, *J. Phys. Chem. C*, 2010, **114**, 21694.
36 J. Yahia, *Phys. Rev.*, 1963, **130**, 1711.
37 H. P. R. Frederikse, *J. Appl. Phys.*, 1961, **32**, 2211.
38 T. Kolodiazhnyi, A. Petric, M. Niewczas, C. Bridges, A. Safa-Sefat and J. E. Greedan, *Phys. Rev. B: Condens. Matter Mater. Phys.*, 2003, **68**, 5.
39 J. J. Kasinski, L. A. Gomez-Jahn, K. J. Faran, S. M. Gracewski and D. Miller, *J. Chem. Phys.*, 1989, **90**, 1253.
40 C. Kormann, D. W. Bahnemann and M. R. Hoffmann, *J. Phys. Chem.*, 1988, **92**, 5196.
41 E. Hendry, F. Wang, J. Shan, T. F. Heinz and M. Bonn, *Phys. Rev. B: Condens. Matter Mater. Phys.*, 2004, **69**, 1.
42 E. Yagi, R. Hasiguti and M. Aono, *Phys. Rev. B: Condens. Matter Mater. Phys.*, 1996, **54**, 7945.
43 P. Gorai, A. G. Hollister and E. G. Seebauer, *ECS J. Solid State Sci. Technol.*, 2012, **1**, Q21.
44 R. Vaidyanathan, M. Y. L. Jung, R. D. Braatz and E. Seebauer, *AIChE J.*, 2006, **52**, 366.
45 P. Kofstad, *J. Phys. Chem. Solids*, 1962, **23**, 1579.
46 J. F. Marucco, J. Gautron and P. Lemasson, *J. Phys. Chem. Solids*, 1981, **42**, 363.
47 J. R. Akse and H. B. Whitehurst, *J. Phys. Chem. Solids*, 1978, **39**, 457.
48 P. Erhart, A. Klein and K. Albe, *Phys. Rev. B: Condens. Matter Mater. Phys.*, 2005, **72**, 85213.
49 P. Erhart and K. Albe, *Phys. Rev. B: Condens. Matter Mater. Phys.*, 2006, **73**, 115207.
50 P. Erhart and K. Albe, *Appl. Phys. Lett.*, 2006, **88**, 201918.
51 R. Vaidyanathan, M. Y. L. Jung and E. G. Seebauer, *Phys. Rev. B: Condens. Matter Mater. Phys.*, 2007, **75**, 195209.
52 M. Y. L. Jung, R. Gunawan, R. D. Braatz and E. G. Seebauer, *J. Electrochem. Soc.*, 2004, **151**, G1.
53 K. Gilliard, *Surface Chemistry To Control Bulk Reaction Dynamics of Native Point Defects in Rutile Titanium Dioxide*, 2017.
54 M. Bowker and R. A. Bennett, *J. Phys.: Condens. Matter*, 2010, **22**, 59801.
55 M. Li and E. G. Seebauer, *J. Phys. Chem. C*, 2017, DOI: 10.1021/acs.jpcc.7b09962.
56 Z. Wang and E. G. Seebauer, *Appl. Surf. Sci.*, 2001, **181**, 111.
57 E. G. Seebauer, A. C. F. Kong and L. D. Schmidt, *Surf. Sci.*, 1988, **193**, 417.
58 J. A. McCaulley, R. J. Shul and V. M. Donnelly, *J. Vac. Sci. Technol. A Vacuum, Surfaces, Film.*, 1991, **9**, 2872.
59 R. Madix and J. Schwartz, *Surf. Sci.*, 1971, **24**, 264.

